

# A mid-infrared view of the inner parsecs of the Seyfert galaxy Mrk 1066 using CanariCam/GTC

C. Ramos Almeida<sup>1,2\*</sup>, A. Alonso-Herrero<sup>3†</sup>, P. Esquej<sup>4</sup>, O. González-Martín<sup>1,2</sup>, R. A. Riffel<sup>5</sup>, I. García-Bernete<sup>1,2</sup>, J. M. Rodríguez Espinosa<sup>1,2</sup>, C. Packham<sup>6</sup>, N. A. Levenson<sup>7</sup>, P. Roche<sup>8</sup>, T. Díaz-Santos<sup>9</sup>, I. Aretxaga<sup>10</sup>, C. Álvarez<sup>1,2</sup>

<sup>1</sup>*Instituto de Astrofísica de Canarias, Calle Vía Láctea, s/n, E-38205, La Laguna, Tenerife, Spain*

<sup>2</sup>*Departamento de Astrofísica, Universidad de La Laguna, E-38206, La Laguna, Tenerife, Spain*

<sup>3</sup>*Instituto de Física de Cantabria, CSIC-Universidad de Cantabria, E-39005, Santander, Spain*

<sup>4</sup>*Departamento de Astrofísica, Facultad de CC. Físicas, Universidad Complutense de Madrid, E-28040, Madrid, Spain*

<sup>5</sup>*Departamento de Física, CCNE, Universidade Federal de Santa Maria, 97105-900 Santa Maria, RS, Brazil*

<sup>6</sup>*Department of Physics and Astronomy, University of Texas at San Antonio, One UTSA Circle, San Antonio, USA*

<sup>7</sup>*Gemini Observatory, Casilla 603, La Serena, Chile*

<sup>8</sup>*Department of Physics, University of Oxford, Oxford OX1 3RH, UK*

<sup>9</sup>*Spitzer Science Center, California Institute of Technology, MS 220-6, Pasadena, CA 91125, USA*

<sup>10</sup>*Instituto Nacional de Astrofísica, Óptica y Electrónica (INAOE), 72000 Puebla, México*

## ABSTRACT

We present mid-infrared (MIR) imaging and spectroscopic data of the Seyfert 2 galaxy Mrk 1066 obtained with CanariCam (CC) on the 10.4 m Gran Telescopio CANARIAS (GTC). The galaxy was observed in imaging mode with an angular resolution of  $0.24''$  (54 pc) in the Si-2 filter ( $8.7 \mu\text{m}$ ). The image reveals a series of star-forming knots within the central  $\sim 400$  pc, after subtracting the dominant active galactic nucleus (AGN) component. We also subtracted this AGN unresolved component from the 8–13  $\mu\text{m}$  spectra of the knots and the nucleus, and measured equivalent widths (EWs) of the 11.3  $\mu\text{m}$  Polycyclic Aromatic Hydrocarbon (PAH) feature which are typical of pure starburst galaxies. This EW is larger in the nucleus than in the knots, confirming that, at least in the case of Mrk 1066, the AGN dilutes, rather than destroys, the molecules responsible for the 11.3  $\mu\text{m}$  PAH emission. By comparing the nuclear GTC/CC spectrum with the *Spitzer*/IRS spectrum of the galaxy, we find that the AGN component that dominates the continuum emission at  $\lambda < 15 \mu\text{m}$  on scales of  $\sim 60$  pc (90–100%) decreases to 35–50% when the emission of the central  $\sim 830$  pc is considered. On the other hand, the AGN contribution dominates the 15–25  $\mu\text{m}$  emission (75%) on the scales probed by *Spitzer*/IRS. We reproduced the nuclear infrared emission of the galaxy with clumpy torus models, and derived a torus gas mass of  $2 \times 10^5 M_{\odot}$ , contained in a clumpy structure of  $\sim 2$  pc radius and with a column density compatible with Mrk 1066 being a Compton-thick candidate, in agreement with X-ray observations. We find a good match between the MIR morphology of Mrk 1066 and the extended Pa $\beta$ , Br $\gamma$  and [O III] $\lambda$ 5007 emission. This coincidence implies that the 8.7  $\mu\text{m}$  emission is probing star formation, dust in the narrow-line region, and the oval structure previously detected in the near-infrared. On the other hand, the *Chandra* soft X-ray morphology does not match any of the previous, contrary to what it is generally assumed for Seyfert galaxies. A thermal origin for the soft X-ray emission, rather than AGN photoionization, is suggested by the different data analyzed here.

**Key words:** galaxies: active – galaxies: nuclei – galaxies: Seyfert – galaxies: individual (Mrk 1066) – infrared: galaxies.

## 1 INTRODUCTION

The interplay between nuclear activity and star formation in galaxies is still not well established. There is theoretical

\* Marie Curie Fellow. E-mail: cra@iac.es

† Augusto González Linares Senior Research Fellow

and observational evidence for active galactic nuclei (AGN) quenching star formation through the so-called AGN feedback (see e.g. Granato et al. 2004; Ho 2005; Springel et al. 2005; Schawinski et al. 2007, 2009), but the physical scales on which this quenching takes place, if it does, are not clear yet. Indeed, star formation is detected on kpc-scales down to tens of parsecs from the AGN in Seyfert galaxies (Diamond-Stanic & Rieke 2010, 2012; LaMassa et al. 2012; Alonso-Herrero et al. 2014; Esquej et al. 2014), and numerical simulations predict a relation with some scatter between the star formation rates (SFRs) on different galaxy scales (between 10 kpc and 1 pc) and the black hole accretion rates (Hopkins & Quataert 2010).

Ground-based mid-infrared (MIR) observations with 8–10 m-class telescopes might hold the key for disentangling the relation between nuclear activity and star formation on parsec-scales. The limited spatial resolution of the *Spitzer* Space Telescope (hereafter *Spitzer*;  $\sim 4\text{--}5''$ ) only allows to study this relation on kpc-scales, although with extremely good sensitivity. Therefore, we are conducting a MIR imaging and spectroscopic survey of  $\sim 100$  local AGN using the instrument CanariCam (CC; Tesesco et al. 2003) on the 10.4 m Gran Telescopio CANARIAS (GTC), in La Palma. The sample includes both high-to-intermediate luminosity AGN (PG quasars, radio galaxies and Seyfert galaxies) and low-luminosity AGN (low-ionization nuclear emission-line regions; LINERs) covering almost six orders of magnitude in AGN luminosity (see Alonso-Herrero et al. 2013 for further details).

Among the galaxies in our survey already observed with GTC/CC, we selected the Seyfert 2 (Sy2) Mrk 1066 (UGC 2456), for which there is evidence in the literature of circumnuclear star formation as well as extended NIR line emission (e.g. Pa $\beta$ , Br $\gamma$ , [Fe II]; Riffel et al. 2010). This barred galaxy, at a distance of 47.2 Mpc, has been extensively studied at different wavelengths (Bower et al. 1995; Ramos Almeida et al. 2009a; Smirnova et al. 2010; Riffel et al. 2010; Riffel & Storchi-Bergmann 2011). Our goal is to understand the different mechanisms responsible for the MIR emission in the central kpc of Mrk 1066, including emission from the dusty torus, dust emission from the narrow-line region (NLR) and star formation. In Alonso-Herrero et al. (2014) we present a complementary, detailed study of the extended PAH emission of five local AGN, including Mrk 1066, using GTC/CC spectroscopy. The latter work focuses on star formation only, and seeks for general results on PAH destruction/dilution by the intense AGN continuum.

The presence of on-going star formation in the central kiloparsec of Mrk 1066 was clearly revealed by integral field spectroscopic data from the Near-Infrared Integral Field Spectrometer (NIFS) on the 8 m Gemini North telescope. The data was obtained using adaptive optics (AO), which provided an angular resolution of  $\sim 0.1\text{--}0.2''$  ( $\sim 35$  pc; Riffel et al. 2010; Riffel & Storchi-Bergmann 2011), and showed line-emitting gas elongated in the same direction of the [O III] and the radio emission (PA=315 $^\circ$ ). From the NIR emission line kinematics, Riffel & Storchi-Bergmann (2011) reported the existence of a compact rotating disc of  $\sim 70$  pc radius and an outflow with the same orientation as the radio jet.

The emission-line ratios measured by Riffel et al. (2010)

along the ionization cones are typical of Seyfert galaxies, indicating that the active nucleus is the dominant source of ionization in the NLR, with some contribution from shock excitation. On the other hand, away from the ionization cones the line ratios are characteristic of star-forming regions. These findings explain the results from optical and near-infrared (NIR) data at lower spatial resolution (Bower et al. 1995; Ramos Almeida et al. 2009a), in which we observe a mixture of high and low ionization regions.

Mrk 1066 then offers the perfect scenario for studying the interplay between nuclear activity and star formation in the inner  $\sim 400$  pc of the galaxy, by comparing our new GTC/CC imaging and spectroscopic observations with available multifrequency data of similar resolution.

Throughout this paper we assume a cosmology with  $H_0 = 73 \text{ km s}^{-1} \text{ Mpc}^{-1}$ ,  $\Omega_m = 0.27$ , and  $\Omega_\Lambda = 0.73$ .

## 2 OBSERVATIONS AND DATA REDUCTION

### 2.1 GTC/CC imaging and spectroscopy

The Sy2 galaxy Mrk 1066 was observed in August 2013 with the MIR camera/spectrograph CanariCam (CC). CC uses a Raytheon  $320 \times 240$  Si:As detector which covers a field-of-view (FOV) of  $26'' \times 19''$  on the sky and its pixel scale is  $0.0798''$  (hereafter  $0.08''$ ). The standard MIR chopping-nodding technique was used to remove the time-variable sky background, the thermal emission from the telescope and the detector  $1/f$  noise, where  $f$  is the frequency of the noise component. The employed chopping and nodding throws were  $15''$ , with chop and nod position angles of 45 and  $-135$  deg respectively.

Both imaging and spectroscopic observations were done in queue mode, on different nights and under photometric conditions. The data were taken as part of an ESO/GTC large programme (182.B-2005) awarded 180 hours of GTC/CC time, aimed to conduct a MIR survey of  $\sim 100$  nearby AGN by exploiting the unique capabilities of CC on the GTC. See Alonso-Herrero et al. (2013) for a more detailed description of this MIR survey.

MIR imaging observations of Mrk 1066 were taken on 2013 Aug 27 with GTC/CC, using the narrow Si-2 filter ( $\lambda_c = 8.7 \mu\text{m}$ ,  $\Delta\lambda = 1.1 \mu\text{m}$ ). We took three exposures of 139 s each, which we combined once reduced to produce a single image of 417 s on-source integration time. The airmass during the observations was  $\sim 1.2$ . Images in the same filter of the Point Spread Function (PSF) standard star HD 18449 were obtained immediately after the science target for accurately sampling the image quality, and to allow flux calibration. We measured an angular resolution of  $0.24''$  (54 pc) from the FWHM of the observed PSF standard star.

For the spectroscopy, we employed the low spectral resolution GTC/CC N-band grating, with nominal resolution  $R = \lambda/\Delta\lambda \sim 175$  and covering the spectral range  $7.5\text{--}13 \mu\text{m}$ . The data were taken on 2013 Aug 31 using the  $0.52''$  wide slit, oriented at  $315^\circ$  to make it coincide with the axis of the ionization cones and the radio jet (Bower et al. 1995; Nagar et al. 1999), and passing through the nucleus and the A, B and D knots detected in the NIR (Riffel et al. 2010; see left panel of Figure 1).

We first took an acquisition image in the Si-2 filter to ensure optimal placement of the slit, and after introducing the

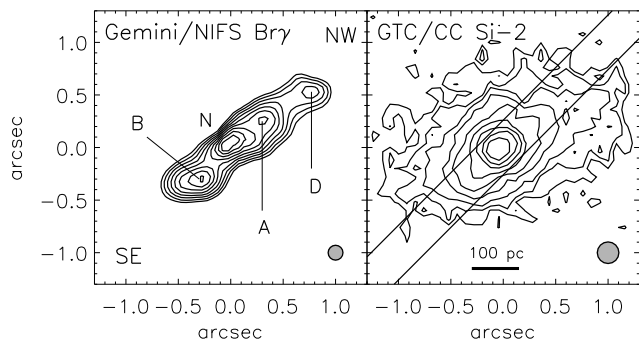


**Figure 1.** Left: Gemini/NIFS 2.166  $\mu\text{m}$  image contours at the  $3\sigma$  level of Mrk 1066 from Riffel et al. (2010), with the position of the active nucleus (N) and the three IR regions detected (A, B and D) indicated. Right: GTC/CC 8.7  $\mu\text{m}$  image contours at the  $3\sigma$  level, with the position of the 0.52'' wide slit superimposed. Both images have been smoothed using a Gaussian function with  $\sigma=0.5$  pixels. Filled circles indicate the approximate angular resolution of the images (0.18'' and 0.24'', respectively).

grating, we integrated for 1061 s on-source at an airmass of  $\sim 1.1$ . Immediately after the observation of Mrk 1066, we obtained a spectrum of the standard star HD 18449 to provide flux calibration and telluric and slit-loss corrections. Using the acquisition images of both the standard star and galaxy nucleus, we measured a FWHM of 0.26'' (58 pc). Thus, the nuclear size is consistent with an unresolved source, although with fainter extended emission.

We reduced the data using the *RedCan* pipeline for the reduction and analysis of MIR imaging and spectroscopic data (González-Martín et al. 2013). In the first step, *RedCan* uses keywords in the fit headers to identify the type of each observing block, and they are used accordingly throughout the pipeline.

In the case of the imaging, *RedCan* uses the Gemini IRAF packages<sup>1</sup>, which include sky subtraction, stacking of the individual images and rejection of bad frames. *RedCan* also provides flux calibrated images when associated standard stars are observed, as it is the case for Mrk 1066. The contours of the fully-reduced GTC/CC 8.7  $\mu\text{m}$  image of Mrk 1066 are shown in the right panel of Figure 1.

For reducing MIR spectra, *RedCan* follows standard MIR reduction recipes, including sky subtraction, stacking of individual observations, rejection of bad frames, wavelength calibration, trace determination and spectral extraction. The latter step can be done either as point source or extended source. In the first case, *RedCan* uses an extraction aperture that increases with wavelength to take care of the decreasing angular resolution, and it also performs a correction to account for slit losses. If the spectrum is extracted as an extended source, a fixed aperture is used and no slit-loss corrections are applied. In this work, we use both the GTC/CC nuclear spectrum extracted as point source and the spectra of the knots (labelled as N, A, B and D in Figure 1), extracted as extended sources (see Sections 3.2

and 3.2.3). *RedCan* finally produces flux-calibrated spectra, which are combined in a single one for each target.

## 2.2 Chandra imaging data

We compiled *Chandra* data of Mrk1066, taken with the Chandra Advanced CCD Imaging Spectrometer (ACIS) on 2003 July 14 (ObsID 4075). The data were reduced from level 2 event files using the CXC *Chandra* Interactive Analysis of Observations (CIAO) software version 4.4. Periods of high background were removed from the observation using the task LC-CLEAN.CL in a source-free region of the sky of the same observation. The net exposure time and net total number of counts in the 0.2-10 keV band are 20 ksec and 800 counts respectively.

*Chandra* data include information on the position where the photons fall into the detector better than the one used with the default pixel size (i.e. 0.492''). Thus, smaller spatial scales are accessible as the image moves across the detector pixel during the telescope dither. This allowed us to sub-pixel binning our images to a pixel size of 0.06''. We extracted two images in the 0.5–2 and 2–10 keV bands and used the adaptive smoothing techniques ASMOOTH to enhance weak structures (Ebeling et al. 2006). This technique is particularly useful for images containing multi-scale complex structures, preserving its spatial signatures. To do that, we selected a minimum and maximum significance S/N level of 1.5 and 3 respectively and a maximum scale of 2 pixels.

## 2.3 Hubble Space Telescope imaging data

We downloaded a reduced [O III] $\lambda 5007$  Å image from the *Hubble* Space Telescope (*HST*) science archive, taken with the Wide Field Planetary Camera (WFPC) on 1992 November 2, as part of *HST* proposal 3724. The data were first published by Bower et al. (1995). The galaxy was observed in the F492M and F547M filters, chosen to isolate the [O III]+H $\beta$  emission and their adjacent continuum, respectively. Using long-slit spectroscopy, Bower et al. (1995) estimated that the [O III] emission accounts for  $\sim 84\%$  of the total emission-line flux in the F492M filter. The pixel scale of the WFPC detector is 0.043''.

## 3 RESULTS

### 3.1 The IR morphology of Mrk 1066

We employed the PSF star, which is a Cohen standard, observed after the 8.7  $\mu\text{m}$  image of Mrk1066 in the same filter, to determine the unresolved (i.e. nuclear) component of Mrk 1066. This is done by scaling the maximum of the PSF star emission to the peak of the galaxy emission, and then integrating all the flux. By doing this, we obtained a nuclear (unresolved) 8.7  $\mu\text{m}$  flux of  $63 \pm 9$  mJy. We estimated a total uncertainty of 15% by quadratically adding the errors in the flux calibration and point source extraction.

Apart from allowing us to determine accurate nuclear fluxes, we use PSF subtraction to study the galaxy's extended emission, after removing the dominant AGN component. We require a flat profile in the residual of the total emission minus the scaled PSF for a realistic, and not

<sup>1</sup> The released version of the Gemini IRAF package is an external package layered upon IRAF and is available to users and other interested parties (<http://www.gemini.edu/sciops/data-and-results/processing-software>)

Knot	(X,Y)	Distance		8.7 $\mu\text{m}$ flux (mJy)
	(arcsec)	(arcsec)	(pc)	
N	(0.00,0.00)	...	...	$63 \pm 9$
A	(-0.38,-0.20)	0.43	100	$3.3 \pm 0.5$
B	(0.27,0.30)	0.40	93	$3.2 \pm 0.5$
D	(-0.79,-0.40)	0.89	207	$2.3 \pm 0.3$

**Table 1.** Positions, projected distances (measured from the nucleus) and fluxes of the four IR regions labelled in Figure 1. Fluxes of knots A, B and D were obtained in  $0.25''$  diameter apertures. The nuclear (unresolved) flux of knot N was obtained from PSF-subtraction, as described in Section 3.1.

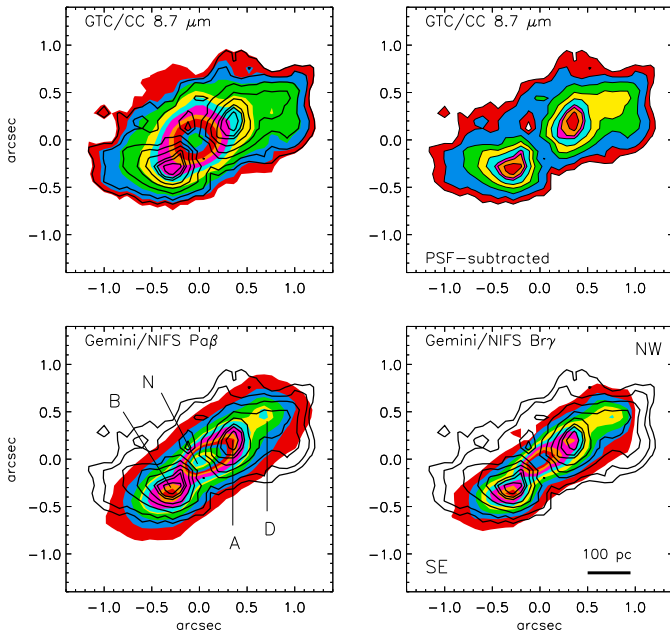


**Figure 2.** Top: GTC/CC  $8.7 \mu\text{m}$  and PSF-subtracted  $8.7 \mu\text{m}$  image contours at the  $3\sigma$  level of Mrk 1066. Bottom: Gemini/NIFS  $\text{Pa}\beta$  and  $\text{Br}\gamma$  contours at the  $3\sigma$  level of Mrk 1066 from Riffel et al. (2010), but interpolated to the pixel size of the GTC/CC images ( $0.08''$ ). Black contours are those of the PSF-subtracted  $8.7 \mu\text{m}$  image. North is up, and east to the left.

over-subtracted, galaxy profile. The residual profiles from the different scalings we tried evidence the best-fitting result, which in this case is 100%. See Radomski et al. (2002) and Ramos Almeida et al. (2009b) for further details.

In Figure 2 we show the GTC/CC  $8.7 \mu\text{m}$  image contours of Mrk 1066 before (top left panel) and after PSF subtraction (top right panel). The PSF-subtracted image reveals a series of MIR knots (labelled in Figure 1 as B, A and D, from SE to NW), which coincide with the position of those seen in the NIR using AO (Riffel et al. 2010). In Table 1 we report the positions of the MIR knots, as measured from the active nucleus (N), and their  $8.7 \mu\text{m}$  fluxes, calculated as described above for the nucleus (PSF-subtraction) and in apertures of  $0.25''$  diameter for knots A, B and D (from the PSF-subtracted image).

In the bottom panels of Figure 2 we show the flux map contours of  $\text{Pa}\beta$  and  $\text{Br}\gamma$  from Riffel et al. (2010). These maps were obtained with the integral field unit of Gemini-

North NIFS and using AO. NIFS has a FOV of  $3'' \times 3''$  and a pixel size of  $0.05''$  was used to construct the flux maps in Riffel et al. (2010), which here we interpolated to match the pixel size ( $0.08''$ ) of GTC/CC. The total exposure time was 4800 s in both the J and K bands ( $\text{Pa}\beta$  and  $\text{Br}\gamma$  respectively).

The Gemini/NIFS integral field data was employed by Riffel et al. (2010) to measure emission-line ratios in each resolution element, as shown in their figure 8. Using the NIR ratios  $[\text{Fe II}]/\text{Pa}\beta$  and  $\text{H}_2/\text{Br}\gamma$ , Riffel et al. (2010) claimed that the gas in knots B and D is predominantly photoionized by starbursts, whereas the nucleus and knot A have typical values of Seyfert galaxies. The NIR spectrum of knot A shown in figure 1 of Riffel et al. (2010) is indeed very similar to the nuclear spectrum, both extracted in apertures of  $0.25'' \times 0.25''$ .

In Figure 3 we show the *Chandra* contours of the hard (2–10 keV) and soft (0.5–2 keV) X-ray emission, once interpolated to the pixel size of the GTC/CC image ( $0.08''$ ), overlaid on the GTC/CC Si-2 image of Mrk 1066. The left panel of Figure 3 reveals a single nucleus emitting in hard X-rays and coinciding with the position of the MIR nucleus. Besides, the hard X-ray contours do not match the MIR morphology when we subtract the PSF component, as shown in the central panel of Figure 3. Thus, we find that the Seyfert-like emission reported by Riffel et al. (2010) for knot A is not associated with a hard X-ray emitting source, as it is the MIR nucleus.

The soft X-ray emission of Mrk 1066, on the other hand, is elongated along a different axis, with a slightly larger PA than the NIR and MIR emission. In addition, it shows three knots towards the NW, which do not coincide with any of the IR knots (see right panel of Figure 3). The soft X-ray knots have 2–10 keV luminosities of  $1.1$ ,  $1.2$  and  $1.9 \times 10^{39} \text{ erg s}^{-1}$ , as measured from the *Chandra* data, the NW knot being the most luminous. These luminosities are in the boundary between those of luminous X-ray binaries and ultra-luminous X-ray sources (ULXs;  $L_X \sim 1 \times 10^{39} \text{ erg s}^{-1}$ , Miller & Colbert 2004; Fabbiano & White 2006; González-Martín et al. 2006).

Considering the availability of multiwavelength archival data publicly available for Mrk 1066, of similar angular resolution, we use them to assess the importance of recent star formation activity, NLR dust and shocks in the inner  $\sim 400$  pc of the galaxy. This is discussed in detail in Section 4.1.

### 3.2 Nuclear and extended IR emission

In Figure 4 we show the nuclear spectrum of Mrk 1066, extracted as a point source. There is a good agreement between the flux calibration of the nuclear spectrum provided by *RedCan* and the nuclear  $8.7 \mu\text{m}$  flux obtained from the imaging in Section 3.1, as we only measured a 15% mismatch between the two. For consistency, we scaled the spectrum to the nuclear flux obtained from the CC image and we estimated a 15% total uncertainty for the CC spectrum by quadratically adding the errors in the flux calibration and point source extraction.

The most intense feature in the GTC/CC nuclear spectrum shown in the left panel of Figure 4 is the  $11.3 \mu\text{m}$  PAH band, which reveals the presence of star formation in the central  $\sim 60$  pc. The  $8.6 \mu\text{m}$  PAH feature is weaker, although it

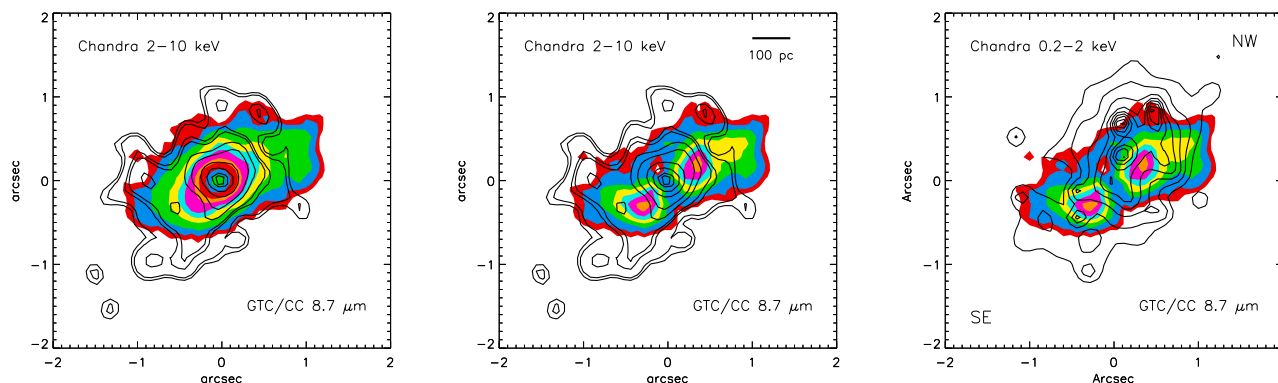


**Figure 3.** Left and center: contours, at the  $3\sigma$  level, of the hard (2–10 keV) X-ray emission of Mrk 1066 (black lines), overlaid on the GTC/CC 8.7  $\mu\text{m}$  contours (in colour) before and after subtracting the PSF. Right: same as in the central panel, but with the contours of the soft (0.5–2 keV) X-ray emission overlaid. The *Chandra*/ACIS images were interpolated to the pixel size of GTC/CC ( $0.08''$ ).

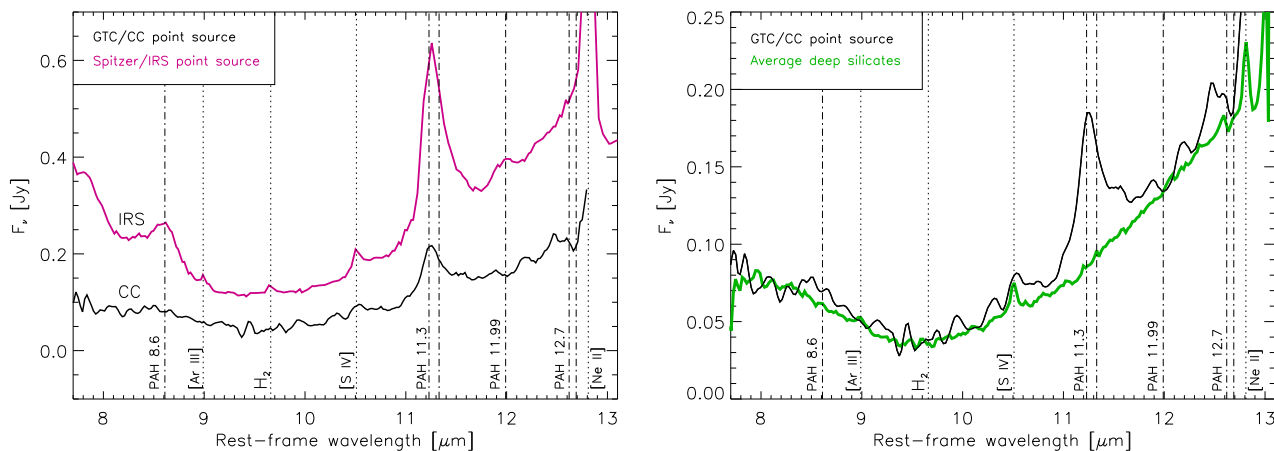


**Figure 4.** Left: Nuclear GTC/CC N-band and IRS/*Spitzer* spectra (black and pink lines respectively) of Mrk 1066. Both spectra have been extracted as point sources, which corresponds to the central  $\sim 60$  and  $\sim 830$  pc respectively. Right: Comparison between the nuclear GTC/CC spectrum and the stacked nuclear spectrum of the seven galaxies with relatively deep silicate features in Esquej et al. (2014), scaled at 12  $\mu\text{m}$ . In both panels, the vertical dotted lines indicate the position of typical star-forming regions/AGN emission lines/bands.

becomes more conspicuous in the  $0.52'' \times 2''$  spectrum shown in figure 1 in Alonso-Herrero et al. (2014).

For comparison, in the left panel of Figure 4 we show the *Spitzer*/Infrared Spectrograph (IRS) spectrum, retrieved from Cornell Atlas of *Spitzer*/IRS Source (CASSIS v4; Lebouteiller et al. 2011). The spectrum was obtained in staring mode with the short-low (SL) module, which covers the range  $\sim 5$ –15  $\mu\text{m}$  and provides spectral resolution  $R = 60$ –120. Considering the typical angular resolution of  $3.7''$  for the SL module, given by the slit width, this corresponds to a physical scale of 830 pc. This is 14 times larger than the physical scale probed by the CC spectrum, of  $\sim 60$  pc. The *Spitzer*/IRS spectrum shows prominent 8.6 and 11.3  $\mu\text{m}$  PAH features, as well as intense [Ne II] $\lambda 12.81$   $\mu\text{m}$  and relatively weak [S IV] $\lambda 10.51$   $\mu\text{m}$  (see left panel of Figure 4).

In the right panel of Figure 4 we compare the nuclear GTC/CC spectrum of Mrk 1066 and the stacked spectrum of the seven galaxies with relatively deep silicate features in Esquej et al. (2014). This stacking was done using nuclear N-band spectra from the Gemini instruments T-ReCS and

MICHELLE of Sy2 galaxies in the RSA sample, which also probe spatial scales of  $\sim 60$ –65 pc. From this comparison, it is clear that the 9.7  $\mu\text{m}$  silicate feature that we detect in the GTC/CC nuclear spectrum of Mrk 1066 is among the deepest reported in Esquej et al. (2014). By performing a linear fitting of its adjacent continuum (using the two featureless regions 8–8.2  $\mu\text{m}$  and 12–12.2  $\mu\text{m}$ ), we measured an apparent optical depth of the silicate feature  $\tau_{9.7} = 1.11$ . This value is among the largest reported for a sample of nearby Seyfert galaxies by González-Martín et al. (2013), measured from Gemini/T-ReCS data. In particular, it is coincident with the  $\tau_{9.7}$  values measured for NGC 3281, NGC 5506 and NGC 7582, which are edge-on galaxies with nuclear dust lanes. Mrk 1066 has an intermediate inclination, but its foreground extinction in the nucleus is also high ( $A_V \sim 5$  mag; Riffel et al. 2010) and could be contributing to the silicate absorption.

Parameter	Prior	Median	MAP
$\sigma$	[15°, 75°]	62° $\pm$ 5	68°
$Y$	[5, 100]	33 $\pm$ 31	19
$N_0$	[1, 15]	12 $\pm$ 2	13
$q$	[0, 3]	0.8 $\pm$ 0.6	0.2
$i$	[0°, 90°]	35° $\pm$ 21	17°
$\tau_V$	[5, 150]	66 $\pm$ 10	72
$A_V$	[4, 6] mag	5.2 $\pm$ 0.5	5.7 mag
$R_o$	...	3 $\pm$ 4 pc	2 pc
$L_{bol}^{AGN}/10^{43}$	...	6.0 $\pm$ 2.2	5.2 $erg s^{-1}$
$N_H^{torus}/10^{23}$	...	7.0 $\pm$ 1.4	7.1 $cm^{-2}$
$M_{torus}/10^5$	...	2.2 $\pm$ 4.5	1.7 $M_\odot$

**Table 2.** Clumpy model parameters, intervals considered as uniform priors, median and MAP values of the posteriors resulting from the fit of Mrk 1066 nuclear SED. Parameters: width of clouds angular distribution ( $\sigma$ ), radial extent of the torus ( $Y$ ), number of clouds along equatorial ray ( $N_0$ ), index of the radial density profile ( $q$ ), inclination angle of the torus ( $i$ ), optical depth per single cloud ( $\tau_V$ ) and foreground extinction ( $A_V$ ).

### 3.2.1 Nuclear SED modelling with clumpy torus models

Recent success in explaining several properties of the nuclear IR spectral energy distributions (SEDs) of Seyfert galaxies has been gathered under the assumption of a clumpy distribution of dust surrounding AGN (Mason et al. 2009; Nikutta et al. 2009; Ramos Almeida et al. 2009b, 2011b,c; Hönic & Kishimoto 2010; Alonso-Herrero et al. 2011, 2012a, 2013; Lira et al. 2013).

*BayesClumpy*<sup>2</sup> (Asensio Ramos & Ramos Almeida 2009, 2013) is a computer program that can be used to fit photometry and/or spectra with the clumpy dusty torus models of Nenkova et al. (2008a,b). The fitting is done in a Bayesian scheme, carrying out inference over the model parameters for observed SEDs. Therefore we can specify a-priori information about the model parameters. We consider the priors to be truncated uniform distributions for the six model parameters in the intervals reported in Table 2. See Ramos Almeida et al. (2014) for a detailed description of the model parameters and examples of SED fitting with *BayesClumpy*.

We fitted the nuclear SED of Mrk 1066 considering reprocessed torus emission and foreground extinction ( $A_V$ ). This extinction is introduced as another prior in the fit, and it accounts for additional dust along the line-of-sight (LOS), unrelated to the torus. Riffel et al. (2010) presented extinction maps obtained from their integral field NIR data (using the Pa $\beta$ /Br $\gamma$  line ratio), and reported values ranging from  $\sim$ 4 to 5.6 mag in the innermost region of Mrk 1066. Thus, we considered the prior  $A_V=[4,6]$  mag in our fit and the IR extinction curve of Chiar & Tielens (2006).

The fitted SED includes an *HST*/NICMOS 1.6  $\mu$ m nuclear flux (0.51 $\pm$ 0.16 mJy; Quillen et al. 2001), the GTC/CC 8.7  $\mu$ m nuclear flux (63 $\pm$ 9 mJy) and the GTC/CC spectrum, scaled to the latter flux. We resampled the spectrum to  $\sim$ 40 points, following the same methodology as in Alonso-Herrero et al. (2013), and we did not include the spectral regions containing PAH emission bands in the fit.

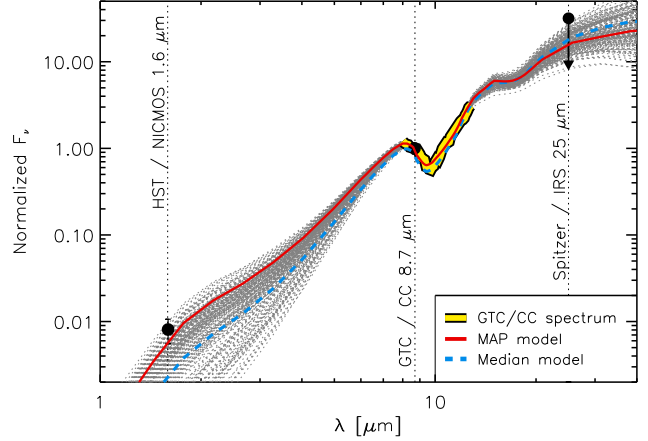


**Figure 5.** High spatial resolution IR SED of Mrk 1066 (thick yellow line: GTC/CC nuclear spectrum; black dots: *HST*/NICMOS 1.6  $\mu$ m flux from Quillen et al. 2001, GTC/CC 8.7  $\mu$ m flux from this work and *Spitzer*/IRS 25  $\mu$ m flux from Sargsyan et al. 2011), normalized to the 8.7  $\mu$ m point. Solid red and dashed blue lines correspond to the MAP and median models respectively. Grey curves are the clumpy models sampled from the posterior and compatible with the data.

Finally, we used the 25  $\mu$ m *Spitzer*/IRS flux reported in Sargsyan et al. (2011) as an upper limit (2001 mJy) to constrain the longest MIR wavelengths.

The result of the fitting process of the IR SED are the posterior distributions for the six parameters that describe the models (defined in Table 2),  $A_V$  and the vertical shift required to match the fluxes of a chosen model to an observed SED. These posteriors are shown in Figure A1 in Appendix A. We can also translate the results into corresponding spectra, as shown in Figure 5. The red solid line corresponds to the best-fitting model, described by the combination of parameters that maximizes the posterior (maximum-a-posteriori, MAP). The blue dashed line represents the model computed with the median value of each parameter posterior. Finally, the grey dotted lines are all the clumpy SEDs reconstructed from the model parameters sampled from the posterior, i.e. all the models that are compatible with the observations. We refer the reader to Asensio Ramos & Ramos Almeida (2009, 2013) for further details on the Bayesian formalism.

It is clear from Figure 5 that the MAP model is the one that better reproduces the observed data. In the following we will refer to MAP values, although the medians, with their corresponding errors, are also reported in Table 2 and shown in Figure A1 in Appendix A.

An estimation of the AGN bolometric luminosity can be obtained from the vertical shift applied to the models to fit the data, which we allow to vary freely (see Ramos Almeida et al. 2009a, 2011b and Alonso-Herrero et al. 2011 for details). Using this shift, we obtain  $L_{bol}^{AGN} = 5.2 \times 10^{43} \text{ erg s}^{-1}$ , a value that can be compared with the bolometric luminosity estimated from the 2-10 keV luminosity. Marinucci et al. (2012) reported a bolometric luminosity  $L_{bol}^{X-ray} = 1.3 \times 10^{44} \text{ erg s}^{-1}$ , once con-

<sup>2</sup> <https://github.com/aasensio/bayesclumpy>

verted to our cosmology<sup>3</sup>. This luminosity was obtained using a large aperture, which contains part of the extended X-ray emission detected by *Chandra* (see Section 4.1). Using the *Chandra* data described in Section 2.2, we extracted a nuclear X-ray spectrum of the central 0.85'', and estimated a 2–10 keV luminosity of  $1.5 \times 10^{40} \text{ erg s}^{-1}$ . Using the same correction factors as in Marinucci et al. (2012), we obtain  $L_{bol}^{X\text{-ray}} = 2.0 \times 10^{43} \text{ erg s}^{-1}$ . Therefore,  $L_{bol}^{AGN}$  derived from the fitted clumpy torus model is intermediate between the value reported by Marinucci et al. (2012) and the estimation from *Chandra* data calculated in this work.

Using the MAP value of the optical extinction produced by the torus along the LOS ( $A_V^{torus} = 375 \text{ mag}$ ), we can derive the column density of the obscuring material using the Galactic dust-to-gas ratio ( $N_H^{torus} = 1.9 \times 10^{21} \times A_V^{torus}$ ; Bohlin et al. 1978). This gives  $N_H^{torus} = 7.1 \times 10^{23} \text{ cm}^{-2}$  (see Table 2), which is compatible with X-ray observations showing that Mrk 1066 is a Compton-thick candidate (Shu et al. 2007).

We can also estimate the torus gas mass from the fit, which in turn is a function of  $\sigma$ ,  $N_0$ ,  $\tau_V$ ,  $R_{sub}$  and  $Y$  (see Section 6.1 in Nenkova et al. 2008b). Using the MAP values reported in Table 2, we estimate  $M_{torus} = 1.7 \times 10^5 M_\odot$ . This is the gas mass in a clumpy torus of  $\sim 2 \text{ pc}$  radius, which is orders of magnitude smaller than the sizes probed by CO observations of Mrk 1066 obtained with the 30 m single-dish IRAM telescope, which correspond to 24 kpc ( $M_{H_2} = 2.7 \times 10^9 M_\odot$ ; Kandalyan 2003). Riffel & Storchi-Bergmann (2011) also estimated a gas mass of  $M_{H_2} = 3.6 \times 10^7 M_\odot$  for the  $\sim 70 \text{ pc}$  radius circumnuclear disk of Mrk 1066 using the Gemini/NIFS data. This value is still much larger than the torus mass estimated from our modelling, but again, we are talking about scales that differ almost two orders of magnitude. As a comparison, we can look at the gas masses reported by Hicks et al. (2009) for the inner parsecs of a sample of nearby Seyfert galaxies obtained from VLT/SINFONI measurements of the H<sub>2</sub>1-0S(1) line at 2.1  $\mu\text{m}$ . In the case of the Circinus galaxy, another Sy2 but at 4 Mpc distance only, they reported  $M_{H_2} = 1.9 \times 10^6 M_\odot$  in a radius of 9 pc. This value is more comparable to Mrk 1066's, probing similar spatial scales ( $\sim 2 \text{ pc}$  radius). More recently, García-Burillo et al. (2014) reported a gas mass of  $1.2 \times 10^5 M_\odot$  for NGC 1068 (10 pc radius), using new CO(6-5) band 9 observations from the Atacama Large Millimeter/submillimeter Array (ALMA).

It is noteworthy the low torus inclination with respect to our LOS ( $i=17^\circ$ ). If we look at figure 15 in Riffel & Storchi-Bergmann (2011), which shows a scheme of the inner  $\sim 600 \text{ pc}$  of Mrk 1066, we can see that the ionization cones are not exactly in the plane of the sky, which immediately implies a torus inclination different than edge-on ( $i=90^\circ$ ). The NW cone is indeed above the plane of the galaxy, whilst the SE cone is underneath. This picture is consistent with the kinematic modelling presented in Fischer et al. (2013). They reported a small opening angle for the ionization cones ( $\theta=25^\circ$ ) that agrees with the estimation from *HST*/WFPC observations of Mrk 1066

(Bower et al. 1995) and with the large torus width derived from our modelling ( $\sigma=68^\circ$ ). However, Fischer et al. (2013) reported a nearly edge-on torus inclination angle ( $i=80^\circ$ ), very different to ours. We repeated the fit with clumpy torus models forcing  $i$  to vary between  $60^\circ$  and  $90^\circ$ , but the results do not reproduce the *HST*/NICMOS data point (the fitted models underestimate the NIR flux). In either way, the MAP torus model shown in Figure 5 and the one resulting from the more restrictive  $i$  prior only differ 9–12% between 6 and 30  $\mu\text{m}$ , which is the maximum wavelength range considered in the following Sections.

### 3.2.2 AGN+SB spectral decomposition fits

Taking advantage of the nuclear SED fitting with clumpy torus models performed in Section 3.2.1, we can estimate the AGN contribution to the MIR emission of Mrk 1066 on the spatial scales probed by the *Spitzer*/IRS 5–38  $\mu\text{m}$  and the GTC/CC 7.5–13  $\mu\text{m}$  spectra ( $\sim 830$  and  $\sim 60 \text{ pc}$  respectively).

We took a simple approach to decompose the *Spitzer*/IRS spectrum shown in Figure 4 into AGN and starburst components. As the AGN template, we used the MAP clumpy torus model shown as a red solid line in Figure 5. The star-forming galaxy templates include the average spectrum of local starbursts of Brandl et al. (2006) and the templates of LIRGs in the range  $\log(L_{IR}/L_\odot) = 10.5\text{--}12$  from Rieke et al. (2009). The fitting procedure is described in detail in Alonso-Herrero et al. (2012b), although they used an iterative method to perform the spectral decomposition, as they did not have the privileged information from high angular resolution data that we do have for Mrk 1066. In our case, we simply tried different combinations of the MAP torus model and the starburst templates, allowing for rescaling of the two components. We finally chose the starburst template that, together with the AGN component, minimized  $\chi^2$ , which corresponds to the  $\log(L_{IR}/L_\odot) = 11.25$  LIRG template from Rieke et al. (2009). The result of the fit for the *Spitzer*/IRS spectrum, with a spatial resolution of 3.7'' (the SL slit width), is shown in the left panel of Figure 6.

The fit was done in the 6–30  $\mu\text{m}$  range to avoid the edges and the slightly decreased signal-to-noise of the longest wavelengths. From Figure 6 we see that, whilst the starburst component dominates at shorter wavelengths ( $\lambda < 15 \mu\text{m}$ ), with 30% of AGN contribution at 6  $\mu\text{m}$ , the AGN becomes dominant for  $\lambda \gtrsim 15 \mu\text{m}$ , reaching 75% at 15–25  $\mu\text{m}$ . At longer wavelengths, the AGN contribution smoothly decreases. This is consistent with the results found by Mullaney et al. (2011) for a sample of intermediate-luminosity AGN ( $L_{2-10\text{keV}} \sim 10^{42-44} \text{ erg s}^{-1}$ ), whose 6–100  $\mu\text{m}$  SEDs are best described by a broken power-law (representative of the AGN emission) that generally peaks between 15 and 20  $\mu\text{m}$ , and falls steeply at  $\gtrsim 40 \mu\text{m}$ . In the case of Mrk 1066, the starburst component becomes dominant again at  $\lambda > 30 \mu\text{m}$  (see left panel of Figure 6).

The AGN contribution that we measured for Mrk 1066 at 15–25  $\mu\text{m}$ , in the scales probed by *Spitzer*/IRS (3.7''), is among the largest reported by Alonso-Herrero et al. (2012b) for a volume-limited complete sample of 53 nearby LIRGs, which is representative of the local LIRG population. Mrk 1066 is nearly a LIRG with a Seyfert nucleus, if

<sup>3</sup> Marinucci et al. (2012) used a correction factor of 70 for obtaining the intrinsic 2–10 keV luminosity, as Mrk 1066 is a Compton-thick candidate.

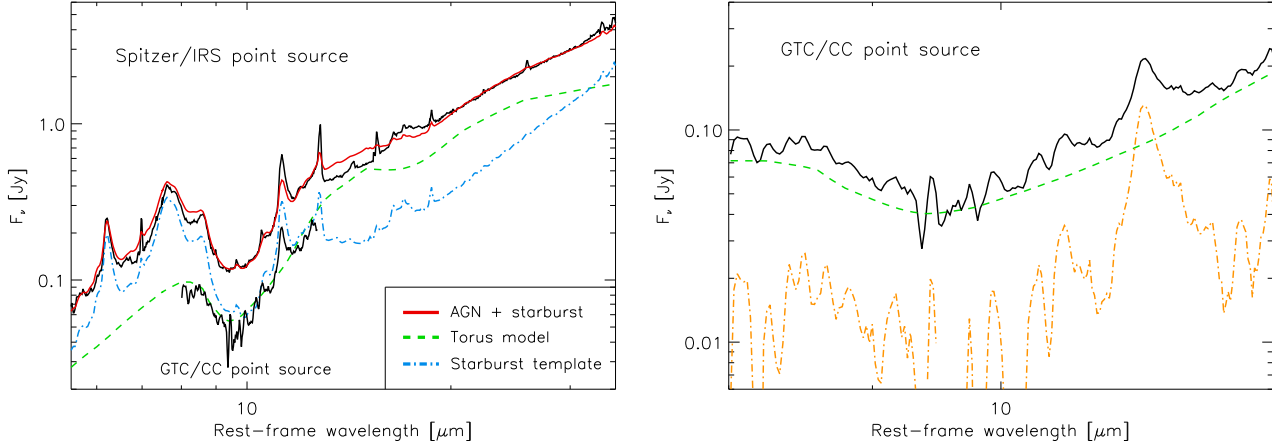


**Figure 6.** Left: Spectral decomposition of the *Spitzer*/IRS spectrum extracted as point source. Black lines are the rest-frame *Spitzer*/IRS and GTC/CC spectra. Green dashed and blue dot-dashed lines are the MAP torus model and the chosen starburst template respectively. Red solid line is the sum of the fitted starburst and AGN component. Right: GTC/CC spectrum and MAP torus model (solid black and green dashed lines respectively). Orange dot-dashed line corresponds to the residual from subtracting the MAP torus model from the GTC/CC nuclear spectrum.

we consider the IR luminosity reported by Sargsyan et al. (2011), once converted to our cosmology,  $\log(L_{IR}/L_{\odot})=10.9$ . Using this value, we can estimate the AGN bolometric contribution to the IR luminosity,  $L_{bol}^{X-ray}/L_{IR}=0.43^4$ . Therefore, Mrk 1066 belongs to the 8% of local LIRGs studied in Alonso-Herrero et al. (2012b) that have a significant AGN bolometric contribution to the IR luminosity ( $L_{bol}^{X-ray}/L_{IR} > 0.25$ ), which are indeed those classified as Seyferts.

In the left panel of Figure 6 we also show the GTC/CC 8–12.7  $\mu\text{m}$  spectrum, extracted as point source, for comparison. Without applying any scaling, the GTC/CC spectrum coincides with the AGN component obtained from the *Spitzer*/IRS fit. This is expected, as, by definition, the AGN component always has to be the same. In the right panel of Figure 6 we plot the GTC/CC nuclear spectrum and the MAP torus model in Figure 5. According to the fit performed in Section 3.2.1, the AGN contribution on the scales probed by the GTC/CC spectrum ( $\sim 60$  pc) dominates the nuclear MIR emission, varying between 90% and 100%, depending on the wavelength (we chose two featureless regions of the spectra, centred at 8.2 and 12  $\mu\text{m}$ ). The dot-dashed line in the right panel of Figure 6 corresponds to the residual from subtracting the MAP torus model from the GTC/CC nuclear spectrum.

The contribution from star formation to the nuclear GTC/CC spectrum of Mrk 1066 (i.e. the inner  $0.26'' \times 0.52'' \approx 60 \text{ pc} \times 120 \text{ pc}$ ) is mainly concentrated on the PAH features at 8.6 and 11.3  $\mu\text{m}^5$ , as it can be seen from the right panel of Figure 6. Whilst the contribution of

star formation to the weaker 8.6  $\mu\text{m}$  emission is only  $\sim 20\%$ , the 11.3  $\mu\text{m}$  band is mostly due to star formation ( $\sim 60\%$ ). In the case of the *Spitzer*/IRS 3.7'' aperture, the starburst contribution to the two PAH features is  $\sim 70\%$ .

Summarizing, for the case of Mrk 1066, the AGN component dominates the MIR at  $\lambda < 15 \mu\text{m}$  on scales of  $\sim 60$  pc (90–100%), and decreases down to 35–50% when the 8–12.5  $\mu\text{m}$  emission of the central  $\sim 830$  pc is considered<sup>6</sup>. Instead, if we look at longer wavelengths ( $\lambda > 15 \mu\text{m}$ ) the AGN component probed by the *Spitzer*/IRS 3.7'' aperture reaches 75% at 15–25  $\mu\text{m}$  (i.e. at the peak of AGN emission), which is among the highest percentages in the reference sample of LIRGs studied in Alonso-Herrero et al. (2012b).

### 3.2.3 MIR spectroscopy of the knots

From the analysis of the GTC/CC MIR nuclear spectrum of Mrk 1066 it is clear that there is star formation activity taking place in the inner  $\sim 60$  pc of the galaxy. Now we can take advantage of the spatial information afforded by the GTC/CC spectroscopy and extract spectra at the location of knots A, B and D and the nucleus. Thus, we extracted the four spectra as extended sources, centered in the positions listed in Table 1 and using apertures of  $0.52'' \times 0.4''$ . This is the maximum aperture that we can use avoiding overlap between the different knots. These spectra are shown in the left panel of Figure 7. The nuclear spectrum (N) is the brightest, whilst knot D is the dimmest ( $\sim 1''$  NW).

Only in the case of knot D we resolve the double peak of the 11.3  $\mu\text{m}$  PAH feature. Besides, we marginally detect the [S IV]10.5  $\mu\text{m}$  fine structure line in the spectrum of knot A. This line is thought to originate in the NLR, as it is well correlated with [Ne V] and [O IV], and therefore it is widely used as AGN tracer (see Dasyra et al. 2011 and references therein). However, as shown by Pereira-Santaella et al.

<sup>4</sup> Here we use the value of  $L_{bol}^{X-ray}$  from Marinucci et al. (2012), which is consistent with the luminosities used in Alonso-Herrero et al. (2012b). Note that in the case of Mrk 1066, this  $L_{bol}^{X-ray}$  constitutes an upper limit to the real  $L_{bol}^{AGN}$  (see Section 3.2.1).

<sup>5</sup> With the exception of the silicate feature, the clumpy torus models do not account for spectral features.

<sup>6</sup> Also measured at 8.2 and 12  $\mu\text{m}$ .



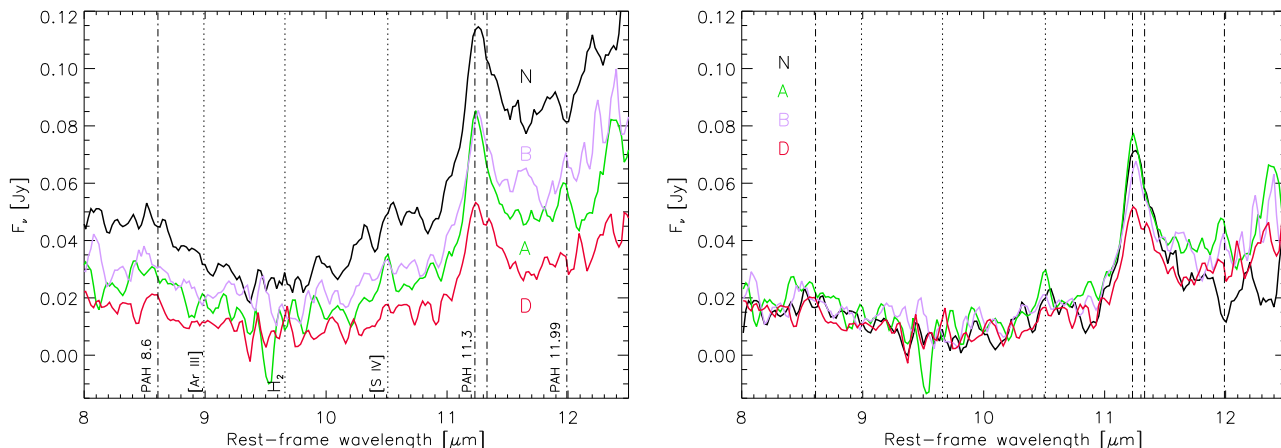


**Figure 7.** Left: GTC/CC N-band spectra of the nucleus (black line) and knots A, B and D (green, purple and red line respectively) extracted as extended sources, using an aperture of  $0.52'' \times 0.4''$  and centered in the positions listed in Table 1. Right: AGN-subtracted GTC/CC N-band spectra of the knots. Vertical dotted lines indicate the position of the emission lines and the PAH features.

(2010), this emission line can be also produced in star-forming regions, due to its low ionization potential (35 eV), similar to that of the  $[\text{O III}]\lambda 5007 \text{ \AA}$  line (Trouille et al. 2011).

The spectra shown in the left panel of Figure 7 have contributions from both AGN and star formation. Therefore, in order to minimize as much as possible the AGN contamination from the spectra of the knots, we estimated the AGN contribution at their positions using the GTC/CC 8.7  $\mu\text{m}$  images, before and after PSF subtraction (see top panels of Figure 2).

We obtained 8.7  $\mu\text{m}$  fluxes in the two images at the positions of the four knots, using the same aperture employed for extracting the spectra ( $0.4''$ ). Then, first we compared the measurements before and after PSF-subtraction and estimated the AGN contribution to the total fluxes in each of the knots. We find that the AGN represents 88%, 16%, 36% and 3% in knots N, A, B and D respectively. Second, we scaled the MAP torus model obtained from the fit of the GTC/CC nuclear spectrum (see Figure 5), to the spectrum of knot N, extracted as an extended source. To do that, we calculated the scale factor between the GTC/CC nuclear spectra (extracted as point and extended source) and applied it to the MAP torus model. Finally, we multiplied the scaled MAP torus model by the percentages obtained from the comparison between the MIR images, and subtracted the AGN component from the spectra of the knots (see Figure 8).

The residuals from the subtraction, i.e. the spectra of the knots without the AGN contribution, are also shown in the right panel of Figure 7. We note that using this method we are just subtracting the unresolved MIR emission, dominated by dust within the torus, but not the extended NLR emission.

The AGN-subtracted spectra of the knots are flatter than those without subtraction (shown in the left panel of Figure 7). This implies that the deep silicate feature observed in the spectrum of the nucleus is partly produced by both the obscuring dusty torus of Mrk1066 and the fore-

ID	$L_{11.3\mu\text{m}}$ ( $\times 10^{41} \text{ erg s}^{-1}$ )	SFR ( $M_{\odot} \text{ yr}^{-1}$ )	EW ( $\mu\text{m}$ )	AGN-sub EW ( $\mu\text{m}$ )
N	$1.31 \pm 0.07$	$0.32 \pm 0.02$	$0.34 \pm 0.02$	$1.89 \pm 0.32$
A	$1.00 \pm 0.06$	$0.25 \pm 0.01$	$0.46 \pm 0.03$	$0.63 \pm_{0.17}^{0.42}$
B	$0.99 \pm 0.06$	$0.25 \pm 0.01$	$0.39 \pm 0.02$	$0.80 \pm_{0.41}^{0.45}$
D	$0.78 \pm 0.05$	$0.19 \pm 0.01$	$0.61 \pm 0.05$	$0.67 \pm_{0.06}^{1.03}$

**Table 3.** Measurements of the 11.3  $\mu\text{m}$  PAH feature in the knots before and after subtracting the AGN contribution. The values of  $L_{11.3\mu\text{m}}$  and SFR before and after AGN subtraction are compatible within the errors. Errors in the last column include the uncertainties associated with AGN subtraction.

ground extinction that we considered in the fit ( $A_V=4-6 \text{ mag}$ ).

We measured the flux and equivalent width (EW) of the 11.3  $\mu\text{m}$  PAH feature in the GTC/CC spectra of the knots before and after subtracting the AGN contribution (shown in Figure 7). We followed the method described in Hernán-Caballero et al. (2011) and implemented for ground-based spectroscopy by Esquej et al. (2014). We fitted a local continuum using two narrow bands (10.75–11  $\mu\text{m}$  and 11.65–11.9  $\mu\text{m}$ ) adjacent to the 11.3  $\mu\text{m}$  PAH feature, and we integrated the flux above the continuum in the rest-frame range 11.05–11.55  $\mu\text{m}$ . Uncertainties are estimated by performing Monte Carlo simulations, as described in detail in Esquej et al. (2014). In the case of the EWs measured from the AGN-subtracted spectra, the errors also include the uncertainties in the fluxes calculated from the GTC/CC 8.7  $\mu\text{m}$  image and the PSF-subtracted 8.7  $\mu\text{m}$  map.

Before subtracting the AGN component from the spectra of the knots, the EW of the 11.3  $\mu\text{m}$  PAH feature is lower in the nucleus than in the knots (see Table 3 and Figure 9). Knot D, which is the most distant from the AGN, shows the largest value of the EW. These values are equal or larger than those reported by Esquej et al. (2014) using the same technique and probing similar scales (e.g.  $\text{EW}_{11.3} = 0.36 \pm 0.02 \mu\text{m}$  for the star-forming Seyfert galaxy NGC 1808).

If we look at the PAH EWs after AGN subtraction (see

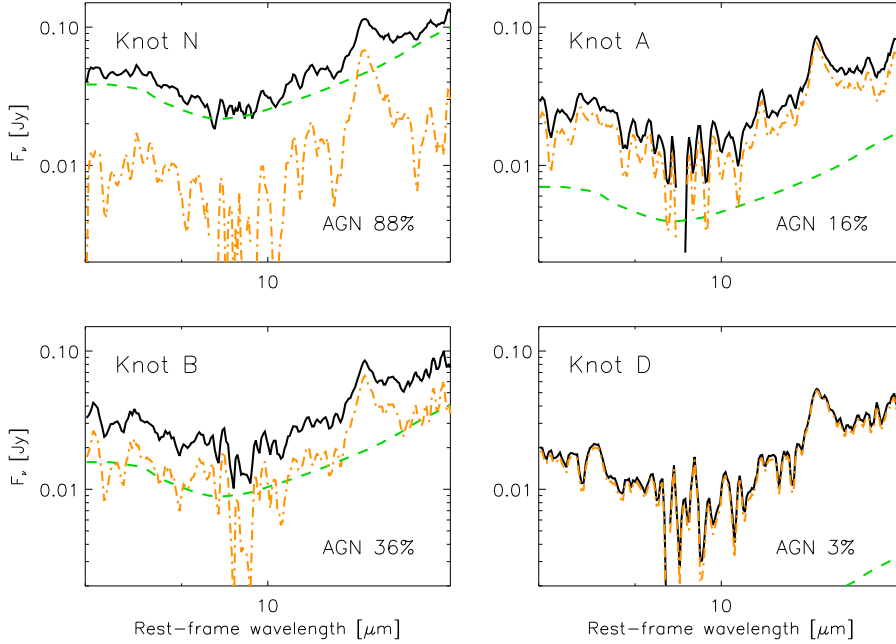


**Figure 8.** Same as the right panel of Figure 6, but for the GTC/CC MIR spectra of the knots, extracted as extended sources. Black lines are the rest-frame spectra, green dashed line is the MAP torus model, once scaled to the percentages indicated in each panel, which correspond to the corresponding AGN contributions. Dot-dashed orange lines are the results from the subtraction of the scaled AGN component (i.e. the green dashed line) from the spectrum of each knot.

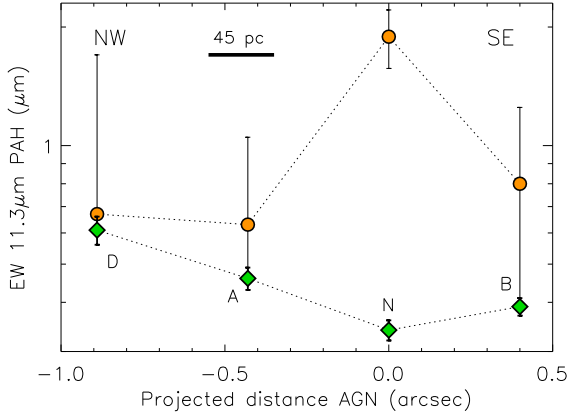


**Figure 9.** Spatial variation of the 11.3  $\mu\text{m}$  PAH feature EW before and after AGN subtraction (green diamonds and orange circles, respectively).

Table 3 and Figure 9), we find that the values increase, specially in the nucleus ( $1.9 \pm 0.3 \mu\text{m}$ ). The lowest EW corresponds to knot A ( $0.6 \pm 0.2^{0.4} \mu\text{m}$ ), and the EW of knot D remains the same within the errors. The nuclear EW is similar to the values reported in figure 6 of Alonso-Herrero et al. (2014) for regions at  $\sim 200\text{--}300$  pc SE and NW of the nucleus ( $1.4\text{--}1.5 \pm 0.3 \mu\text{m}$ )<sup>7</sup>. The EWs measured for knots A, B and D, on the other hand, are lower.

The AGN-corrected EWs are consistent with those mea-

sured for pure starbursts in Hernan-Caballero et al. (2011) and for extra-nuclear star-forming regions in nearby LIRGs (Dıaz-Santos et al. 2010). Thus, here we propose a reliable method to subtract the AGN continuum from MIR spectra, allowing to derive EWs which are representative of star formation.

Finally, using the 11.3  $\mu\text{m}$  PAH luminosities measured for the knots before and after subtracting the AGN contribution from the spectra, we can calculate SFRs following the empirical relation derived in Diamond-Stanic & Rieke (2012):

$$SFR(M_{\odot} \text{ yr}^{-1}) = 9.6 \times 10^{-9} L(11.3 \mu\text{m}; L_{\odot}).$$

The 11.3  $\mu\text{m}$  PAH luminosities and corresponding SFRs are reported in Table 3. Before and after AGN subtraction, we measured SFRs ranging between 0.2 and 0.3  $M_{\odot} \text{ yr}^{-1}$ , which are among the largest values measured by Esquej et al. (2014) for a sample of local Seyfert galaxies in regions of  $\sim 65$  pc in size<sup>8</sup>.

## 4 DISCUSSION

### 4.1 The origin of the circumnuclear emission of Mrk 1066

From the similarity between the MIR images (with and without PSF subtraction) and the Pa $\beta$  and Br $\gamma$  images presented in Section 3.1 (see Figure 2), we can confirm that the GTC/CC Si-2 filter is tracing both emission

<sup>7</sup> We note that Alonso-Herrero et al. (2014) did not subtract the AGN component from the GTC/CC spectra.

<sup>8</sup> Note that neither the luminosities nor the SFRs reported in Table 3 have been multiplied by the factor of two derived by Smith et al. (2007) and used in Esquej et al. (2014).

from the NLR and star formation<sup>9</sup>, and this emission consists on four discrete knots and an extended component. The coincidence between the extended 8.7  $\mu\text{m}$  emission and hydrogen recombination lines is common in IR bright galaxies (Helou et al. 2004; Alonso-Herrero et al. 2006; Díaz-Santos et al. 2008) and it implies that the 8.7  $\mu\text{m}$  emission is due to star formation and/or dust in the NLR in the case of AGN (Radomski et al. 2003; Packham et al. 2005). In the case of Mrk 1066, part of the extended MIR emission could also come from the oval structure of  $\sim 350$  pc radius detected from the emission line kinematics (Riffel & Storchi-Bergmann 2011).

Based on the comparison between the soft X-ray and MIR morphologies of Mrk 1066 (see Figure 3), it seems clear that the soft X-ray emission is not tracing the NLR of this Sy2 galaxy, in contradiction with the most accepted interpretation for its origin. It is generally assumed that the soft X-ray emission of Sy2s is produced by gas photoionized by the nuclear continuum (Kinkhabwala et al. 2002; Ogle et al. 2003; Bianchi et al. 2006; Guainazzi et al. 2007). Using a small sample of eight Sy2 galaxies, Bianchi et al. (2006) compared *Chandra* soft X-ray images with narrow-band optical images obtained with the *HST*, containing the [O III] $\lambda 5007$  Å emission<sup>10</sup>. They found a good coincidence between the soft X-ray and [O III] morphologies, on scales of hundreds of parsecs. However, we find that neither the MIR nor the NIR morphologies, which also trace the NLR emission, as well as star formation, match the soft X-ray emission of Mrk 1066.

In the top left panel of Figure 10 we compare the contours of the soft X-ray emission (in black) with those of the HST/WFPC [O III]+H $\beta$ +continuum Å image (described in Section 2.3). Overall, the soft X-ray emission agrees relatively well with the [O III] emission. However, once we subtract the continuum emission, by using the image taken in the adjacent filter F547N (see top right panel of Figure 10), we find a completely different [O III] morphology, that does not match the soft X-ray emission. Therefore, it would be necessary to compare the continuum-subtracted [O III] and soft X-ray morphologies of a large sample of galaxies to confirm/discard a common source of ionization.

Alternatively, a thermal origin for the extended soft X-ray emission of star-forming active galaxies as Mrk 1066 has been also claimed (see e.g. Levenson et al. 2001), and one third of Sy2 galaxies have been found to have thermal soft X-ray emission (Turner et al. 1997). In the bottom panels of Figure 10 we compare the soft X-ray contours of Mrk 1066 with the Gemini/NIFS [Fe II] $\lambda 1.257$   $\mu\text{m}$  and VLA 3.6 cm maps from Riffel et al. (2010), both showing their peaks of emission along the NW cone.

Strong [Fe II] emission is common in Sy2 galaxies, but there are three mechanisms that can produce it, namely, 1) AGN photoionization, 2) radio jet interactions with the surrounding medium and 3) fast shocks associated with supernova remnants in starburst regions (see Ramos Almeida et al. 2009a and references therein). In the case of Mrk 1066, the peaks of the [Fe II] and radio emission

perfectly match, as shown in Figure 10 and in figure 4 of Riffel et al. (2010), indicating that the [Fe II] emission is at least partly produced by the radio jet interaction with the ISM.

From the bottom right panel of Figure 10 we can see that the three soft X-ray knots are just outside the jet cocoon. Riffel & Storchi-Bergmann (2011) claimed that the outflow of ionized gas to the NW would be produced by the radio jet interaction, with the jet pushing away the ISM material and exciting it. This scenario would explain the increase in velocity dispersion shown in figure 5 of Riffel & Storchi-Bergmann (2011), which exactly coincides with the position of the most luminous soft X-ray knot. Moreover, high velocity [Fe II] gas is detected at the position of the central soft X-ray knot (see figure 4 in Riffel & Storchi-Bergmann 2011), also suggesting a thermal origin for both the [Fe II] and the extended soft X-ray emission.

On the other hand, the NIR and MIR knots are within the cone and the jet, and the extended IR emission is copatial with the NLR emission. In Figure 11 we show the continuum-subtracted [O III] image and the 3.6 cm radio contours, interpolated to the pixel size of the GTC/CC image (0.08"), with the PSF-subtracted 8.7  $\mu\text{m}$  contours overlaid. The [O III] emission is elongated in the same direction as the IR emission. The line-emitting gas of the SE part of the NLR of Mrk 1066 is detected in the NIR and MIR, but not in the optical, and this is likely due to extinction from the foreground galaxy. In fact, Figure 11 completely agrees with the scheme of the central parsecs of the galaxy shown in figure 15 of Riffel & Storchi-Bergmann (2011), in which the SE cone would be obscured by the rotating disk whose major axis coincides with the stellar disk. They claim that the bulk of [O III] emission would be produced in the biconical outflow oriented along the radio jet and ionization cones, as shown in in Figure 11 (PA=315°). Besides, this scheme is also compatible with an intermediate orientation of the obscuring torus, which collimates the emission of the ionization cones (see Section 3.2.1).

We also note that the MIR emission is more extended to the NW than the [O III] emission, indicating that the 8.7  $\mu\text{m}$  emission is not only tracing NLR gas and star formation, but also the oval structure of  $\sim 350$  pc radius detected by Riffel & Storchi-Bergmann (2011) in the NIR. In an attempt to quantify the contribution of the NLR to the extended MIR emission, we performed a GALFIT modelling of the 8.7  $\mu\text{m}$  GTC/CC image, which is described in Appendix B. Unfortunately, because of the almost identical orientations of the NLR and the oval structure detected by Riffel & Storchi-Bergmann (2011) in the NIR (135° and 128° respectively), we cannot separate the two components, as both are included in the Sersic profile used for the fit. We can, however, estimate an upper limit to the luminosity of the NLR by using the integrated flux of the GALFIT model:  $\text{Log } L_{\text{NLR}} \leq 43.20 \pm 0.07 \text{ erg s}^{-1}$ .

Finally, regarding the distribution of the molecular gas in Mrk 1066, as traced by the NIR H<sub>2</sub> lines, Riffel et al. (2010) found it to be more conspicuous at the positions of the nucleus and knot A, and likely produced by X-ray heating of the circumnuclear gas, with some contribution from thermal emission. The influence of shocks in the H<sub>2</sub> emission can be quantified using the H<sub>2</sub>/PAH ratio (Ogle et al. 2010).

<sup>9</sup> The Si-2 filter includes the contribution from the 8.6  $\mu\text{m}$  PAH feature and its underlying continuum.

<sup>10</sup> [O III] is generally used to trace the NLR emission in AGN.

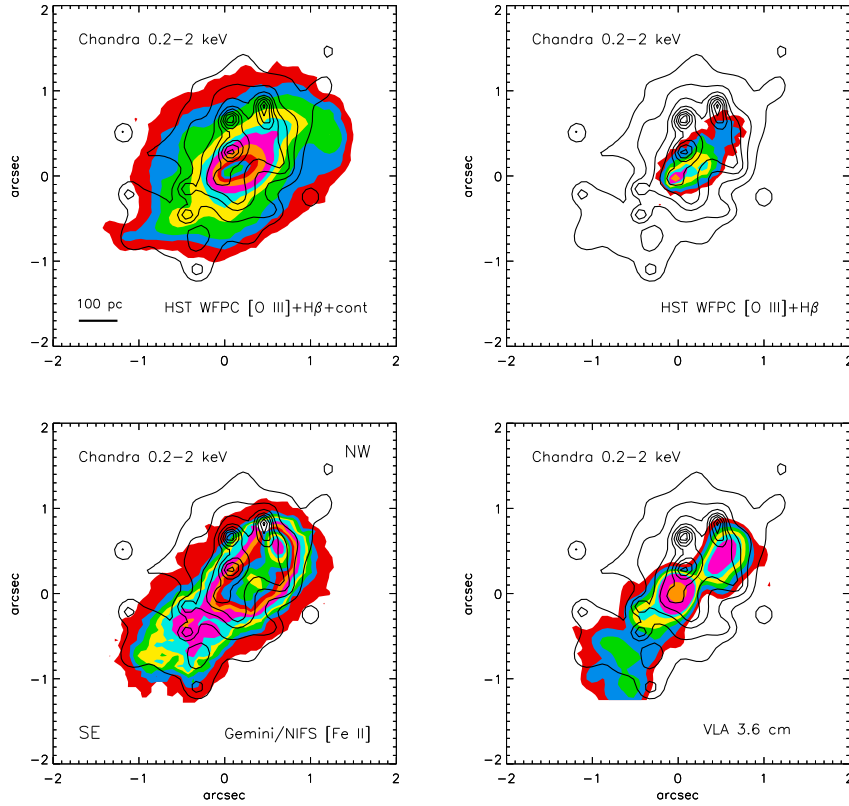


**Figure 10.** Contours of the soft (0.5–2 keV) X-ray emission of Mrk 1066 from *Chandra*/ACIS imaging data (black lines), overlaid on the *HST*/WFPC [O III], continuum-subtracted [O III], Gemini/NIFS [Fe II] $\lambda$ 1.257  $\mu$ m and VLA 3.6 cm contours (in colour). The WFPC, NIFS and VLA images have been interpolated to the pixel size of the *Chandra*/ACIS image (0.06 $''$ ).

Using the emission line fluxes reported by Riffel et al. (2010) for knots N, A and B, and those measured from the PSF-subtracted 8.7  $\mu$ m GTC/CC image using the same aperture (0.25 $''$  diameter), we can study possible variations of the H<sub>2</sub>/PAH ratio in the different knots. We find a larger ratio in knot A: H<sub>2</sub>/PAH=(1.0±0.2)×10<sup>-3</sup>, than in knots N and B: H<sub>2</sub>/PAH=(2.0±0.3)×10<sup>-4</sup> and (5±1)×10<sup>-4</sup> respectively. This is likely related to the radio jet interaction with the ISM, more important towards the NW.

#### 4.2 AGN dilution of the 11.3 $\mu$ m PAH feature

In Section 3.2.3 we presented the spectra of knots N, A, B and D before and after subtracting the AGN contribution that we estimated using the method there described.

Before subtracting the AGN component, the EW of the 11.3  $\mu$ m PAH feature is lower in the nucleus than in the knots (see Table 3 and Figure 9). On the other hand, once we subtract the AGN contribution, the EWs increase (see last column in Table 3), specially in the nucleus. This shows that the relatively low EWs measured before AGN subtraction are due to the increasing AGN continuum as we approach the position of the active nucleus, rather than to PAH destruction. We refer the reader to Alonso-Herrero et al. (2014) for further discussion on AGN dilution of the 11.3  $\mu$ m PAH feature.

The largest increase in EW corresponds to the nucleus (see Figure 9), where AGN dilution is higher. The EWs mea-

sured for knots A and B, which are at distances  $\leq 100$  pc from the nucleus, also experience an increase. Finally, in the case of knot D, at 200 pc NW to the nucleus, AGN dilution is almost negligible, and the EW remains the same within the errors. The EWs measured, after AGN subtraction, for knots A, B and D are lower than those reported by Alonso-Herrero et al. (2014) regions at 200–300 pc SE and NW of the nucleus (1.4–1.5±0.3  $\mu$ m). This is likely due to dilution produced by the NLR emission. Note that here we are just subtracting the unresolved AGN emission, which dominates in the nucleus, but represents  $\leq 36\%$  in the knots. We know from the results presented in Riffel et al. (2010) and this work that there is extended IR emission from dust in the NLR of Mrk 1066, and this emission might be diluting the PAH features in the knots.

Taking advantage of the spatial information afforded by the GTC/CC spectroscopy, we have shown that at least in the case of Mrk 1066, the AGN continuum dilutes, rather than destroys, the PAH features on nuclear scales ( $\sim 60$  pc) and up to  $\sim 100$  pc from the active nucleus. This result is in agreement with the findings of Alonso-Herrero et al. (2014) and Esquej et al. (2014).

## 5 CONCLUSIONS

We present new MIR imaging and spectroscopic observations of the Sy2 galaxy Mrk 1066 at subarcsecond angular

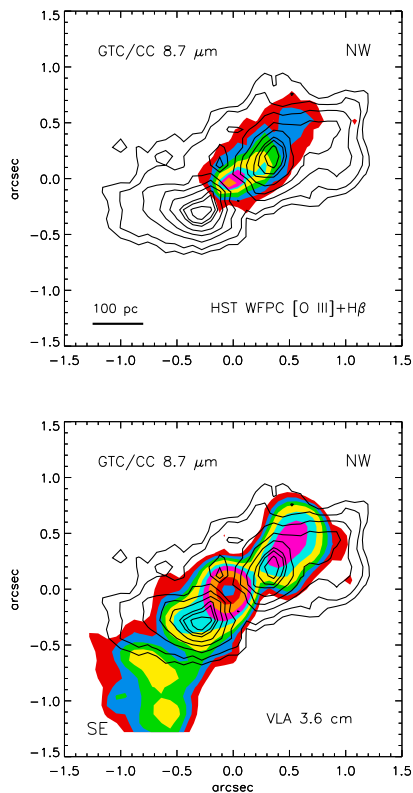


**Figure 11.** Contours of the PSF-subtracted GTC/CC 8.7  $\mu\text{m}$  image (black lines) overlaid on the *HST*/WFPC [O III] continuum-subtracted (top panel) and VLA 3.6 cm colour contours (bottom panel), interpolated to the pixel size of GTC/CC (0.08 $''$ ).

resolution obtained with CanariCam on the 10.4 m GTC. The data probe the central  $\sim 400$  pc of the galaxy with an angular resolution of 54 pc, revealing a series of star-forming knots after subtracting the dominant AGN contribution from the MIR emission. Our major conclusions can be summarized as follows:

- By subtracting the dominant AGN contribution to the GTC/CC nuclear spectrum of Mrk 1066, we find that the EW of the 11.3  $\mu\text{m}$  PAH feature is larger in the nucleus than in the knots, with all of them being typical of starburst galaxies. This confirms that, at least in the case of this galaxy, the AGN does not destroy, but dilutes, the molecules responsible for the 11.3  $\mu\text{m}$  PAH emission in the inner  $\sim 60$  pc of the galaxy and up to  $\sim 100$  pc from the nucleus.
- We measured the flux of the 11.3  $\mu\text{m}$  PAH band in the knots before and after subtracting the AGN contribution to the nuclear spectra, and we find SFRs = 0.2–0.3  $M_{\odot} \text{ yr}^{-1}$ . These values coincide with the largest values measured by Esquej et al. (2014) for local Seyfert galaxies in regions of  $\sim 65$  pc in size.
- We fitted the nuclear NIR and MIR SED of Mrk 1066 with clumpy torus models, and derived a torus gas mass of  $2 \times 10^5 M_{\odot}$ , contained in a clumpy torus of  $\sim 2$  pc radius. Besides, we derived a column density from the fit that is compatible with Mrk 1066 being a Compton-thick candidate, in agreement with X-ray observations.
- By comparing the nuclear GTC/CC MIR spectrum

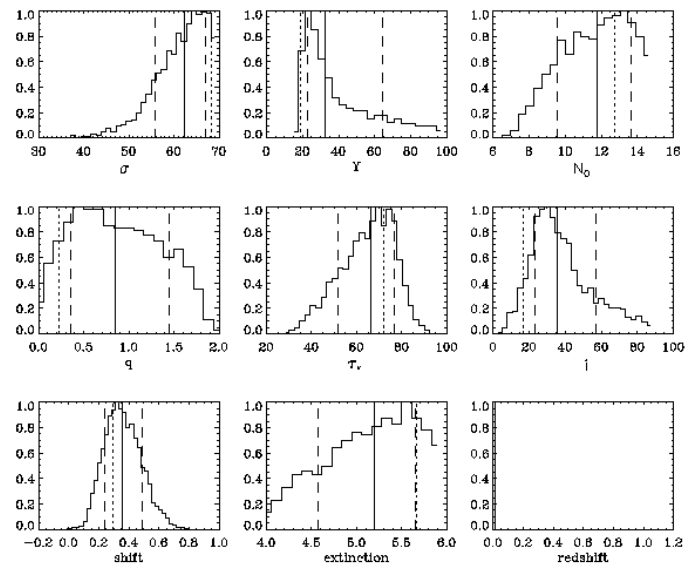


**Figure A1.** Normalized marginal posteriors resulting from the fit of Mrk 1066 nuclear IR SED. Dotted and solid vertical lines represent the MAP and the median of each posterior, respectively, and dashed vertical lines indicate the 68 per cent confidence level for each parameter around the median (see Table 2).

with the *Spitzer*/IRS spectrum of Mrk 1066, and performing spectral decomposition into AGN and starburst components, we find that the AGN component that dominates the continuum emission at  $\lambda < 15 \mu\text{m}$  on scales of  $\sim 60$  pc (90–100%), decreases to 35–50% when the emission of the central  $\sim 830$  pc is considered.

- The AGN contribution to the *Spitzer*/IRS 3.7 $''$  spectrum dominates the MIR emission at 15–25  $\mu\text{m}$  (75%), which is among the highest percentages measured for local LIRGs using the same methodology.
- We find a good match between the MIR morphology and the extended Pa $\beta$ , Br $\gamma$  and [O III] $\lambda 5007$  emission. This coincidence implies that the 8.7  $\mu\text{m}$  extended emission in Mrk 1066 is probing star formation, dust in the NLR, and also the oval structure previously detected in the NIR.
- The *Chandra* soft X-ray morphology does not match either the IR or the [O III] $\lambda 5007$  extended emission, implying that it is not tracing dust in the NLR. Instead, the multi-wavelength data analyzed here favour a thermal origin for the soft X-ray emission.

## APPENDIX A: BAYESIAN INFERENCE.

Here we report the posterior distributions resulting from the fit of the IR SED of Mrk 1066. The top and middle rows of Figure A1 correspond to the posteriors of the six parameters that describe the models (defined in Table 2). The bottom row includes the posteriors of the foreground extinction,  $A_V$ , the vertical shift required to match the fluxes of a chosen model to an observed SED, and the galaxy redshift.

**APPENDIX B: GALFIT MODELLING.**

In order to better characterize the MIR morphology of Mrk 1066, we performed GALFIT (Peng et al. 2002, 2010; version 3.0.5) modelling of the 8.7  $\mu\text{m}$  GTC/CC image. GALFIT is a well-documented two-dimensional fitting algorithm which allows the user to simultaneously fit a galaxy image with an arbitrary number of different model components, and thus to extract structural parameters of the galaxy. The model galaxy is convolved with a PSF and, using the downhill-gradient Levenberg-Marquardt algorithm, is matched to the observational data via the minimization of the  $\chi^2$  statistics.

We used the image of the standard star as PSF component, and the host galaxy was modelled using a Sersic profile to account for the oval structure of  $\sim 350$  pc detected by Riffel & Storchi-Bergmann (2011) in the NIR. All the model parameters were allowed to vary freely except the PSF flux, which we fixed to be the same we obtained from PSF subtraction ( $63 \pm 9$  mJy), and the position angle of the Sersic component ( $128^\circ$ ; Riffel & Storchi-Bergmann 2011). We fixed the flux of the PSF component because otherwise the residual image appeared clearly oversubtracted at the nuclear position. After doing so, the best fit resulted in a Sersic profile with index  $n=0.83$  (i.e., consistent with a disk), effective radius  $R_{eff}=265$  pc and ellipticity  $b/a=0.59$ . The final reduced- $\chi^2$  value is 1.156.

In Figure B1 we display the 8.7  $\mu\text{m}$  GTC/CC contour plots of the central  $670 \times 670$  kpc<sup>2</sup> region of Mrk 1066, the best-fitting model and the model-subtracted residual image. The residuals are overlaid on a colour-scale of the PSF-subtracted MIR image, for comparison. Only the star-forming knots appear in the residual, as the rest of the MIR extended emission is included in the disk model. If we measure the flux of the residual in an aperture of  $2''$  radius, we obtain  $2.5 \pm 0.4$  mJy. This is indicating that the Sersic component is likely including not only the disk emission but also the NLR emission, with the latter traced by the [O III] image shown in Figure 11. This is likely due to the almost identical orientations of the NLR and the disk ( $135^\circ$  and  $128^\circ$ , respectively). Although we cannot separate the two components in the MIR, we can estimate an upper limit to the NLR emission by using the integrated flux of the GALFIT model<sup>11</sup>, which is  $172 \pm 26$  mJy.

**ACKNOWLEDGMENTS**

This research was supported by a Marie Curie Intra European Fellowship within the 7th European Community Framework Programme (PIEF-GA-2012-327934). CRA and IGB acknowledge financial support from the Instituto de Astrofísica de Canarias and the Spanish Ministry of Science and Innovation (MICINN) through project PN AYA2010-21887-C04.04 (Estallidos). IGB is grateful to the PhD contract funded by Fundación La Caixa. AAH acknowledges support from the Spanish Plan Nacional de Astronomía y Astrofísica under grant AYA2012-31447 and from the Augusto G. Linares Program through the Universidad de

Cantabria. RAR thanks the support of Brazilian institutions CNPq and FAPERGS. PE acknowledges support from the Spanish Programa Nacional de Astronomía y Astrofísica under grant AYA2012-31277. CP acknowledges support from UTSA to help enable this research. OGM and JRE acknowledge financial support from the Spanish Ministry of Science and Innovation (MICINN) through project AYA2012-39168-C03-01.

Based on observations made with the Gran Telescopio CANARIAS (GTC), installed in the Spanish Observatorio del Roque de los Muchachos of the Instituto de Astrofísica de Canarias, in the island of La Palma.

This research has made use of the NASA/IPAC Extragalactic Database (NED) which is operated by the Jet Propulsion Laboratory, California Institute of Technology, under contract with the National Aeronautics and Space Administration.

The scientific results reported in this article are based in part on data obtained from the *Chandra* Data Archive.

Based on observations made with the NASA/ESA Hubble Space Telescope, obtained from the data archive at the Space Telescope Science Institute. STScI is operated by the Association of Universities for Research in Astronomy, Inc. under NASA contract NAS 5-26555.

Based on observations obtained at the Gemini Observatory, which is operated by the Association of Universities for Research in Astronomy, Inc., under a cooperative agreement with the NSF on behalf of the Gemini partnership: the National Science Foundation (United States), the Science and Technology Facilities Council (United Kingdom), the National Research Council (Canada), CONICYT (Chile), the Australian Research Council (Australia), Ministério da Ciência e Tecnologia (Brazil) and Ministerio de Ciencia, Tecnología e Innovación Productiva (Argentina).

The authors acknowledge Santiago García Burillo, Andrés Asensio Ramos and Mar Mezcua for useful discussions. Finally, we are extremely grateful to the GTC staff for their constant and enthusiastic support, and to the anonymous referee for useful comments.

**REFERENCES**

- Alonso-Herrero, A., et al. 2014, MNRAS, 443, 2766
- Alonso-Herrero, A., et al. 2013, ApJ, 779, L14
- Alonso-Herrero, A., et al. 2012a, MNRAS, 425, 311
- Alonso-Herrero, A., et al. 2012b, ApJ, 744, 2
- Alonso-Herrero, A., et al. 2011, ApJ, 736, 82
- Alonso-Herrero, A., Colina L., Packham C., Díaz Santos T., Rieke G. H., Radomski J. T., Telesco C., 2006, ApJ, 625, L83
- Asensio Ramos, A., Ramos Almeida, C. 2013, MNRAS, 428, 195
- Asensio Ramos, A., Ramos Almeida, C. 2009, ApJ, 696, 2075
- Bianchi, S., Guainazzi, M., Chiaberge, M. 2006, A&A, 448, 499
- Bohlin, R. C., Savage, B. D., Drake, J. F. 1978, ApJ, 224, 132
- Bower G., Wilson A., Morse J. A., Gelderman R., Whittle M., Mulchaey J., 1995, ApJ, 454, 106
- Brandl, B., et al. 2006, ApJ, 653, 1129

<sup>11</sup> The integrated flux of the model does not include either the nuclear component or the star-forming knots.

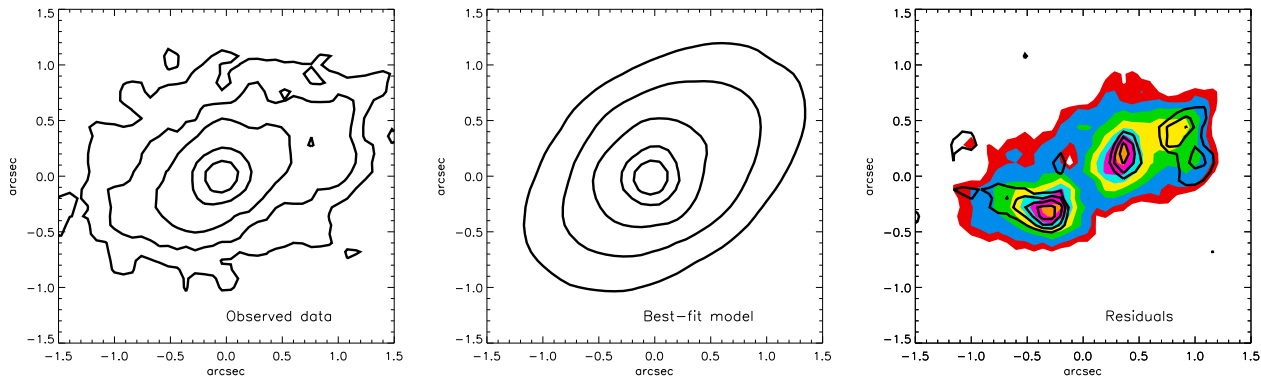


**Figure B1.** From left to right: contours of the 8.7  $\mu\text{m}$  GTC/CC image, the best-fitting model and the model-subtracted residual image. The residuals are overlaid on a colour-scale of the PSF-subtracted MIR image, for comparison.

- Chiar, J. E., Tielens, A. G. G. M. 2006, *ApJ*, 637, 774  
 Dasyra, K. M., et al. 2011, *ApJ*, 740, 94  
 Diamond-Stanic, A. M., Rieke, G. H. 2012, *ApJ*, 746, 168  
 Diamond-Stanic, A. M., Rieke, G. H. 2010, *ApJ*, 724, 140  
 Díaz-Santos T., Alonso-Herrero A., Colina L., Packham C., Levenson, N. A., Pereira-Santaella, M., Roche, P. F., Telesco C., 2008, *ApJ*, 684, 211  
 Díaz-Santos T., Alonso-Herrero A., Colina L., Packham C., Radomski J., Telesco C., 2008, *ApJ*, 684, 211  
 Ebeling, H., White, D. A., Rangarajan, F. V. N. 2006, *MNRAS*, 368, 65  
 Esquej, P., et al. 2014, *ApJ*, 780, 86  
 Fabbiano G., White N. E., 2006, in Lewin W., van der Klis M., eds, *Compact Stellar X-ray Sources*. Cambridge Univ. Press, Cambridge, p. 475  
 Fischer, T. C., Crenshaw, D. M., Kraemer, S. B., Schmitt, H. R. 2013, *ApJS*, 209, 1  
 García-Burillo, S., et al. 2014, *A&A*, 567, 125  
 Granato, G. L., De Zotti, G., Silva, L., Bressan, A. Danese, L. 2004, *ApJ*, 600, 580  
 González-Martín, O., et al. 2013, *A&A*, 553, 35  
 González-Martín, O., Fabian, A. C., Sanders, J. S. 2006, *MNRAS*, 367, 1132  
 Guainazzi, M., Bianchi, S. 2006, *MNRAS*, 374, 1290  
 Helou G., et al. 2004, *ApJS*, 154, 253  
 Hernán-Caballero A., Hatziminaoglou E., 2011, *MNRAS*, 414, 500  
 Hicks, E. K. S., Davies, R. I., Malkan, M. A., Genzel, R., Tacconi, L. J., Müller Sánchez, F., Sternberg, A.  
 Ho, L. C. 2005, *ApJ*, 629, 680  
 Hönig, S. F., Kishimoto, M. 2010, *A&A*, 523, 27  
 Hopkins, P. F., Quataert, E. 2010, *MNRAS*, 407, 1529  
 Kandalyan, R. A. 2003, *A&A*, 398, 493  
 Kinkhabwala, A., et al. 2002, *ApJ*, 575, 732  
 LaMassa, S. M., et al. 2012, *ApJ*, 758, 1  
 Lebouteiller, V., et al. 2011, *ApJS*, 196, 8  
 Levenson, N. A., Weaver, K. A., Heckman, T. M. 2001, *ApJ*, 550, L230  
 Lira, P., Videla, L., Wu, Y., Alonso-Herrero, A., Alexander, D. M., Ward, M. 2013, *ApJ*, 764, 159  
 Marinucci, A., Bianchi, S., Nicastro, F., Matt, G., Goulding, A. D. 2012, *ApJ*, 748, 130  
 Mason R. E., Levenson N. A., Shi Y., Packham C., Gorjian V., Cleary K., Rhee J., Werner M. 2009, *ApJ*, 693, L136  
 Miller, M. C., Colbert, E. J. M. 2004, *Int. J. Mod. Phys.*, 13, 1  
 Mullaney, J. R., Alexander, D. M., Goulding, A. D., Hickox, R. C. 2011, *MNRAS*, 414, 1082  
 Nagar N. M., Wilson A. S., Mulchaey J. S., Gallimore J. F., 1999, *ApJS*, 120, 209  
 Nenkova, M., Sirocky, M. M., Ivezić, Z., Elitzur, M. 2008a, *ApJ*, 685, 147  
 Nenkova, M., Sirocky, M. M., Nikutta, R., Ivezić, Z., Elitzur, M. 2008b, *ApJ*, 685, 160  
 Nikutta, R., Elitzur, M., Lacy, M. 2009, *ApJ*, 707, 1550  
 Ogle, P., Boulanger, F., Guillard, P., Evans, D. A., Antonucci, R., Appleton, P. N., Nesvadba, N., Leipski, C., 2010, *ApJ*, 724, 1193  
 Ogle, P. M., Brookings, T., Canizares, C. R., Lee, J. C., Marshall, H. L. 2003, *A&A*, 402, 849  
 Packham C., et al., 2005, *ApJ*, 618, L17  
 Peng C. Y., Ho L. C., Impex C. D., Rix H.-W., 2002, *AJ*, 124, 266  
 Peng C. Y., Ho L. C., Impex C. D., Rix H.-W., 2010, *AJ*, 139, 2097  
 Pereira-Santaella, M., Alonso-Herrero, A., Rieke, G. H., et al. 2010b, *ApJS*, 188, 447  
 Quillen, A. C., McDonald, C., Alonso-Herrero, A., Lee, A., Shaked, S., Rieke, M. J., Rieke, G. H. 2001, *ApJ*, 547, 129  
 Radomski, J. T., Piña, R. K., Packham, C., Telesco, C. M., De Buizer, J. M., Fisher, R. S., Robinson, A. 2003, *ApJ*, 587, 117  
 Radomski, J. T., Piña, R. K., Packham, C., Telesco, C. M., Tadhunter, C. N. 2002, *ApJ*, 566, 675  
 Ramos Almeida, C., Alonso-Herrero, A., Levenson, N. A., Asensio Ramos, A., Rodríguez Espinosa, J. M., González-Martín, O., Packham, C., Martínez, M. 2014, *MNRAS*, 439, 3847  
 Ramos Almeida, C., et al. 2011a, *ApJ*, 731, 92  
 Ramos Almeida, C., et al. 2011b, *MNRAS*, 417, L46  
 Ramos Almeida, C., Pérez García, A. M., Acosta-Pulido, J. A. 2009a, *ApJ*, 694, 1379  
 Ramos Almeida, C., et al. 2009b, *ApJ*, 702, 1127  
 Rieke, G. H., et al. 2009, *ApJ*, 692, 556  
 Riffel, R. A., Storchi-Bergmann, T., Nagar, N. M. 2010, *MNRAS*, 404, 166  
 Riffel, R. A., Storchi-Bergmann, T. 2011, *MNRAS*, 411, 469

- Sargsyan L., Weedman D., Lebouteiller V., Houck J., Barry D., Hovhannisyan A., Mickaelian A. 2011, *ApJ*, 730, 19
- Schawinski, K., et al. 2009, *ApJ*, 690, 1672
- Schawinski, K., et al. 2007, *MNRAS*, 382, 1415
- Shu, X. W., Wang, J. X., Jiang, P., Fan, L. L., Wang, T. G. 2007, *ApJ*, 657, 167
- Smirnova, A. A., Moiseev, A. V., Afanasiev, V. L. 2010, *MNRAS*, 408, 400
- Smith J. D., et al. 2007, *ApJ*, 656, 770
- Springel, V., Di Matteo, T., Hernquist, L. 2005, *MNRAS*, 361, 776
- Telesco, C. M., Ciardi, D., French, J., et al. 2003, *Proc. SPIE*, 4841, 913
- Trouille, L., Barger, A. J., Tremonti, C. 2011, *ApJ*, 742, 46
- Turner, T. J., George, I. M., Nandra, K., Mushotzky, R. F. 1997, *ApJS*, 113, 23